arXiv:1602.08528v1 [cond-mat.mtrl-sci] 26 Feb 2016

Toward a Comprehensive Model of Snow Crystal Growth: 5. Measurements of Changes in Attachment Kinetics from Background Gas Interactions at -5 C

Kenneth Libbrecht
Department of Physics, California Institute of Technology
Pasadena, California 91125

Abstract. We present measurements of the diffusion-limited growth of ice crystals from water vapor at a temperature of -5 C, in air at a pressure of $p_{air} = 1$ bar. Starting with thin, c-axis ice needle crystals, the subsequent growth morphologies ranged from solid prismatic columns to hollow columns to complex "fishbone" dendritic structures as the supersaturation was increased. We modeled the simpler morphologies using analytical techniques together with a cellular-automata method that yields faceted crystalline structures in diffusion-limited growth. We found that the molecular attachment coefficient α_{prism} on faceted prism surfaces in air at -5 C is substantially lower than that measured at low background air pressure. Our data show that increasing p_{air} from 0.01 to 1 bar reduces α_{prism} by nearly two orders of magnitude at this temperature. In contrast, we find that α_{basil} is essentially unaffected by air pressure over this range. These and other measurements indicate that ice surfaces near the melting point undergo a series of complex structural and dynamical changes with temperature that remain largely unexplained at even a qualitative level.

1 Introduction

Our overarching goal in this series of investigations is to develop a comprehensive model of ice crystal growth from water vapor that can reproduce quantitative growth rates as well as growth morphologies over a broad range of circumstances. Although ice crystal formation has been studied extensively for many decades, our understanding of the fundamental physical processes governing growth behaviors at different temperatures and supersaturations remains remarkably poor [1, 2, 3, 4, 5, 6, 7]. For example, the complex dependence of ice growth morphology on temperature, exhibiting several transitions between plate-like and columnar structures [8, 9], remains essentially unexplained even at a qualitative level, although it was first reported over 75 years ago [1].

To address this problem, we have undertaken an experimental program designed to create small ice crystals with simple morphologies and measure their subsequent growth under carefully controlled conditions, to an extent and accuracy surpassing previous efforts [10, 11, 12, 13, 6, 14]. We model the experimental data using a recently developed cellular-automata numerical method that can generate physically realistic faceted structures in diffusion-limited growth [15, 16, 17, 18, 19, 20]. The comparison between measured and modeled ice crystals then provides valuable information about the attachment kinetics governing ice growth from water vapor. From this information we hope to develop a detailed physical picture of the molecular structure and dynamics of the ice surface during solidification.

2 Ice Growth Measurements in a Dual Diffusion Chamber

The ice growth measurements described in this paper were obtained used the dual diffusion chamber described in [21]. The first of the two diffusion chambers was operated with a high water-vapor supersaturation in air, and in this chamber we grew electrically enhanced ice needles with tip radii ˜100 nm and overall lengths up to 4 mm, with the needle axis oriented along the c-axis of the ice crystal. The needle crystals were then transported to the second diffusion chamber, also operating in air at $p_{air} = 1$ bar, where the temperature and supersaturation were independently controlled, and the subsequent growth was recorded using optical microscopy. A well-defined linear temperature gradient in the second chamber ensured that convection currents were suppressed and that the supersaturation could be accurately modeled. In [22] we describe the supersaturation modeling in more detail, along with a calibration of the supersaturation at the location of the test crystals.

Immediately after an ice needle assembly was moved to the second diffusion chamber, the wire base holding the needles was rotated so a particular test needle was in focus in the microscope, with the needle entirely in the focal plane, as shown in Figure 1. During this transport and focusing step, a thin, frost-covered, horizontal shutter plate was positioned just above the ice needles, reducing the supersaturation below the plate to near zero. Once the test needle was satisfactorily positioned (typically taking 10-30 seconds), the shutter was removed and growth measurements commenced. The supersaturation near the test crystal relaxed back to steady state in a time of order $\tau \approx L^2/D \approx$ 5 seconds, where $L \approx 1$ cm is the shutter size and $D \approx 2 \times 10^{-5}$ m^2/sec is the diffusion constant for water vapor in air.

For all the measurements described below, the air temperature was maintained at $T_{center} = -5 \pm 0.1$ C, as determined by a small calibrated thermistor that was frequently placed at the center of the diffusion chamber, at the same location as the tips of the ice needles during their growth. The supersaturation was adjusted by changing the linear temperature gradient inside the diffusion chamber. In particular, the top and bottom temperatures were maintained at $T_{center} \pm \Delta T$, and the supersaturationr was proportional to ΔT^2, as described in [21, 22]. The supersaturation calibration presented in [22] gives $\sigma_{center} \approx 0.00148\,(\Delta T)^2$ when $T_{center} = -5$ C, where σ_{center} is the supersaturation far from the growing ice crystals. The supersaturation $\sigma_{surface}$ at the ice surface must be determined by diffusion modeling.

In a typical growth run at -5 C (measuring a single needle crystal), still photos were taken periodically to record the growth after the shutter was removed. For supersaturations $\sigma_{center} < 2$ percent surrounding the growing crystals, ice needles grew slowly into solid, prismatic columnar structures. The morphology changed with increasing σ_{center}, yielding predominantly hollow columns at $\sigma_{center} \approx 4$ percent, as shown in Figure 1. At still higher σ_{center}, the corners of a hollow column separated to yield needle-like crystals, and a sextet of "fishbone" crystals [23, 21] appeared when $\sigma_{center} > 15$ percent.

The work presented here is limited to $\sigma_{center} < 4$ percent, so the growth morphologies all exhibited solid or hollow columnar morphologies. The diffusion-limited growth of these structures could be quantitatively modeled using a 2D cylindrically symmetric cellular automata code, as described in [18], thus avoiding the need for a full 3D code.

The columnar radius at the end of an ice needle as a function of time, $R(t)$, was extracted directly from the image data. The optical microscope used to photograph the crystals had a resolving power of 2.5 μm, and the image pixels measured 0.85 μm. Our diameter resolution was found to be about ± 2 μm, giving measurements of $R(t)$ that were accurate to about ± 1 μm. We did not distinguish the different "radii" of a projected hexagonal structure in our image data, and this limited the absolute

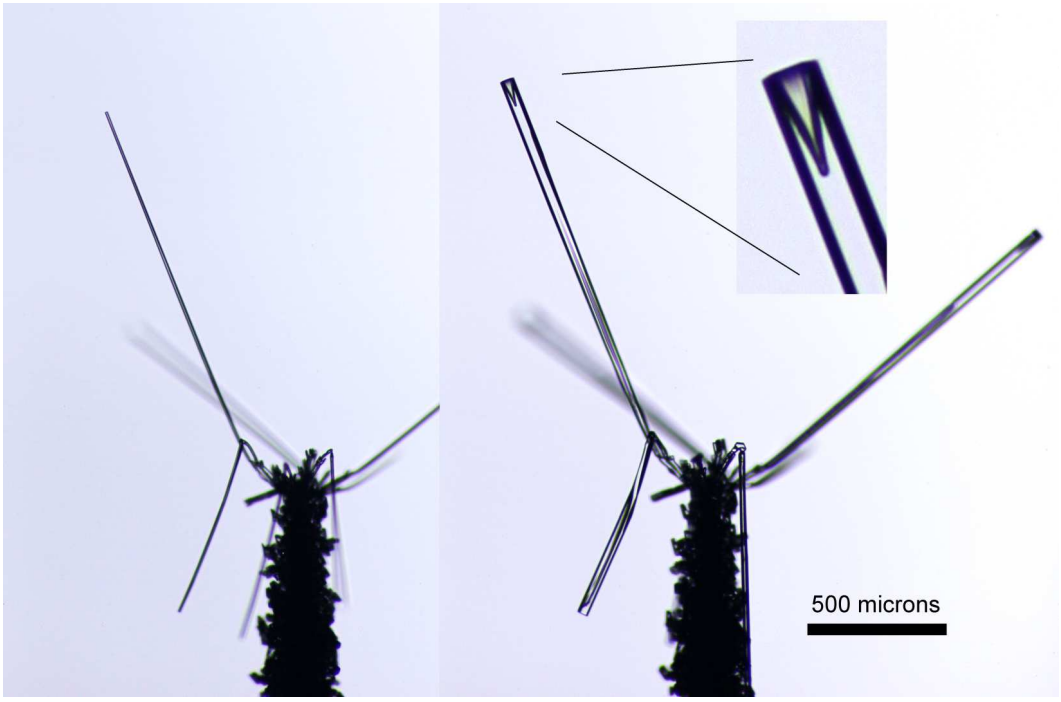

Figure 1: This composite photograph shows an example of a hollow columnar crystal grown at -5 C. The image in the left panel was taken soon after several thin, c-axis "electric" ice needles had grown out from the wire substrate covered in frost crystals. Focusing on a single needle, the right panel shows its structure after an additional nine minutes of growth at a supersaturation of $\sigma_{center} \approx 3.7$ percent (for this particular example). The magnified inset image shows the columnar hollowing that developed as the crystal grew. The diameter and length of the ice column as a function of time were extracted from a set of similar images.

accuracy of our measurements of $R(t)$ to ± 5 percent. Moreover, the faceted needles often did not remain perfectly hexagonal in cross section as they grew, adding additional systematic errors arising from our cylindrically symmetric modeling of the $R(t)$ data.

The height of a needle, $H(t)$, was measured with respect to a "base reference" that consisted of one or more reference points in the frost cluster covering the wire substrate at the base of the needle (for example, see Figure 1). The quality and stability of the base references varied from run to run, and the accuracy of the $H(t)$ measurements was limited to about ± 2 μm by growth of the ice crystals in the base reference with time.

With our dual chamber apparatus, we observed the growth of many crystals over a broad range of T_{center} and ΔT, including many at $T_{center} = -5$ C. Overall, needle crystals grown under similar conditions yielded similar morphologies and growth data. However, variations in the exact value of ΔT, the length and angle of the initial needle, the needle morphology, the amount of frost on the wire substrate, and the location of neighboring crystals, resulted in some run-to-run variability in σ_{center} and other growth parameters. For purposes of clarity, therefore, we restrict the quantitative

analysis described below to just a few individual crystals of exceptional quality. Data from additional crystals confirmed our principal conclusions, but are not presented here.

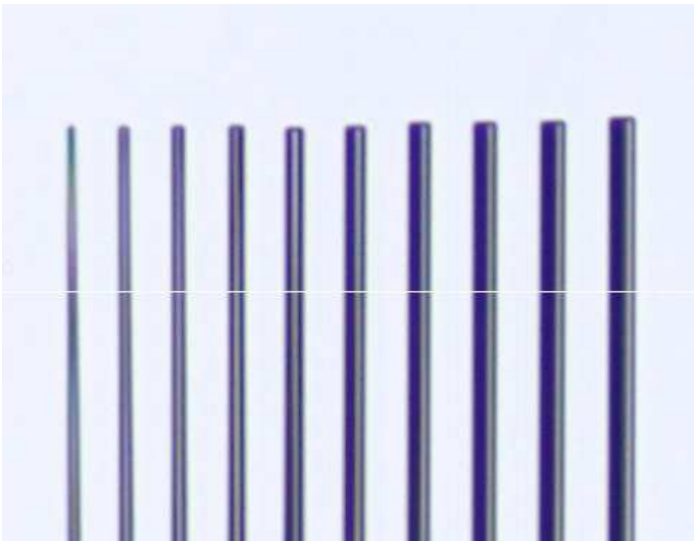

Figure 2: This composite image shows the growth of a simple columnar ice crystal in air at a supersaturation of $\sigma_{center} = 0.92$ percent. The columnar radius and height as a function of time were extracted from these calibrated optical images, yielding the measurements in Figure 3. (These images correspond to every other data point in the graph.) A horizontal white line is drawn 100 μm below the tips of the first several columns.

2.1 Solid Columnar Growth at Low Supersaturation

Figure 2 shows raw imaging data of a solid columnar crystal as it grew in air with $\Delta T = 2.5$ C, for which our supersaturation calibration yields $\sigma_{center} \approx 0.92$ percent [22]. Figure 3 shows the measured $R(t)$ and $H(t)$ data obtained from the full set of images (of which Figure 2 shows a subset), along with model calculations described below. Close inspection of the images revealed that the initial needle exhibited a "positive" taper, with the tip of the needle having the smallest radius. We measured that the needle sides were tilted with respect to the c-axis by $dR/dz \approx 0.007$ at $t = 0$, becoming essentially fully faceted (with the dR/dz measurements extrapolating to zero) by about $t \approx 300$ seconds.

To model $R(t)$, we approximate the crystal as an infinitely long cylinder, which has the growth velocity [22]

$$\frac{dR}{dt} = \frac{\alpha_{diffcyl}\alpha_{cyl}}{\alpha_{diffcyl} + \alpha_{cyl}} v_{kin}\sigma_{center} \tag{1}$$

where α_{cyl} gives the attachment coefficient on the cylindrical surface and

$$\alpha_{diffcyl} = \frac{1}{B}\frac{X_0}{R_{in}}, \tag{2}$$

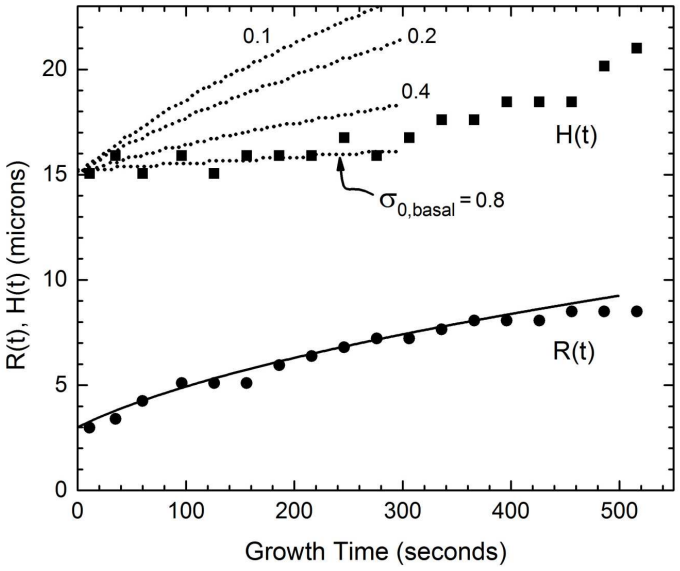

Figure 3: The data points in this graph show measurements of $R(t)$ and $H(t)$ extracted from image data including the images shown in Figure 2. A constant length was subtracted from the $H(t)$ measurements to obtain the (arbitrary) starting point $H(t = 0) \approx 15$ μm. The various lines are from diffusion modeling described in the text.

with $B = \log(R_{far}/R_{in})$ and $X_0 = c_{sat}D/c_{ice}v_{kin} \approx 0.142$ μm [22]. Using $R_{far} = 2$ cm and $R_{in} = R(t) \approx 6$ μm yields $\alpha_{diffcyl} \approx 0.003$.

The needle taper indicates a vicinal surface (inclined slightly from a faceted prism surface) that includes many molecular steps on the sides of the needle, so we expect a rather high attachment coefficient $\alpha_{vicinal}$. Assuming $\alpha_{cyl} = \alpha_{vicinal} \gg \alpha_{diffcyl}$, we can write the cylindrical growth rate more simply as

$$\frac{dR}{dt} = \alpha_{diffcyl} v_{kin} \sigma_{center} \tag{3}$$

which integrates to

$$R(t) = \left[\frac{2X_0 v_{kin} \sigma_{center}}{B} (t - t_0) + R_0^2 \right]^{1/2} \tag{4}$$

Using the measured initial condition $R_0 = 3$ μm at $t = t_0 = 0$ then yields the solid curve shown in Figure 3. The value of σ_{center} was adjusted slightly to fit the data, consistent with measured run-to-run variations of about ± 15 percent. Note that the calibrated σ_{center} obtained in [22] includes effects from crystal heating and incorporates (to a reasonable approximation) differences between an infinitely long cylinder and a more realistic half-infinite cylinder.

Observing that the solid curve provides a good fit to the measured $R(t)$ data in Figure 3 supports our initial assumption that $\alpha_{vicinal} \gg \alpha_{diffcyl}$. This is not a surprising result, because $\alpha_{diffcyl} \approx 0.003$ is quite small compared to our expectation for a vicinal (unfaceted) surface. However, we can

say little more about $\alpha_{vicinal}$ from the $R(t)$ data. If $\alpha_{vicinal} \gg \alpha_{diffcyl}$, then the radial growth is strongly diffusion-limited, so $R(t)$ is essentially independent of $\alpha_{vicinal}$.

Modeling $H(t)$ cannot be done analytically, as the area of the basal surface at the top of the column is small, and the growth is not limited entirely by diffusion. Instead we use the cylindrically symmetric cellular automata method described in [18] to numerically solve the diffusion equation. This treats the hexagonal column as a cylindrical column of finite length, thus allowing us to model the tip growth.

Previous data described in [24] provide a measurement of the basal attachment coefficient, giving $\alpha_{basal} \approx \exp(-\sigma_{0,basal}/\sigma_{surface})$, where $\sigma_{surface}$ is the supersaturation at the basal surface and $\sigma_{0,basal} \approx 0.8$ percent at $T = -5$ C. We therefore tried models with this same functional form, but with $\alpha_{0,basal} = 0.1$, 0.2, 0.4, and 0.8 percent, yielding the model curves for $H(t)$ shown in Figure 3. (The model curves for $R(t)$ are not shown in Figure 3, as they were all nearly identical to the analytic result for $R(t)$.) Other model parameters included: $\alpha_{vicinal} = 0.1$ and $\sigma_{out} = 0.3$ percent on the outer boundary at $R_{out} = 75$ μm. (Note that $\sigma_{out} < \sigma_{center}$ because $R_{out} < R_{far}$ and $\sigma_{center} = \sigma(R_{far})$ [22].)

As can be seen in Figure 3, the $H(t)$ data are in good agreement with the previously measured $\sigma_{0,basal} \approx 0.8$ percent. We also explored models covering a sensible range of other parameters, again concluding that the data are consistent with $\sigma_{0,basal} \approx 0.8$ percent, supporting the previous measurements of α_{basal} in [24]. However, the fact that $\alpha_{vicinal}$ is not well determined limits our ability to measure $\alpha_{0,basal}$ with high accuracy.

The astute reader may notice that the $H(t)$ data in Figure 3 trend upward significantly starting at $t \approx 300$ seconds, which coincides with the formation of faceted prism surfaces. Indeed, the growth behavior does undergo a transition with the appearance of prism facets, indicating $\alpha_{prism} \ll \alpha_{vicinal}$. This phenomenon is better seen at higher growth rates, which we examine next.

2.2 Transitional Growth at Intermediate Supersaturation

The needle growth behavior at -5 C becomes more intriguing when the supersaturation is increased, and we next examine a crystal grown at $\Delta T = 3.5$ C, giving $\sigma_{center} \approx 1.8$ percent at the location of the tip of the needle. The raw images look quite similar to the previous data set (shown in Figure 2) with an initially tapered needle and no hollowing at the solid columnar tip for the duration of the run.

Measurements obtained from the images are shown in Figure 4, revealing a rather abrupt transition in the growth behavior occurring in the interval $t \approx 100 - 160$ seconds, during which the radial growth rate dR/dt diminishes by about a factor of two while the axial growth rate dH/dt increases by a factor of four. Moreover, the raw images show that the needle exhibits a clear positive taper for $t < 100$ seconds, while the columnar sides appear to be faceted prism surfaces soon thereafter.

For $t < t_{transition} \approx 130$ seconds, the observed needle taper suggests that the radial growth is described by $\alpha_{vicinal} \gg \alpha_{diffcyl}$, as we assumed in the low-σ_{center} crystal above. Using this assumption, we can again calculate the radial growth using Equation 4, giving the solid curve shown in Figure 5. The good fit to the data for $t < t_{transition}$ is consistent with our assumption that $\alpha_{vicinal} \gg \alpha_{diffcyl} \approx 0.003$, but otherwise gives us little additional information about the magnitude of $\alpha_{vicinal}$. The value of σ_{center} needed to fit the data was consistent with expectations from our calibration measurements [22].

The fact that the $t > t_{transition}$ data deviate from the analytic $R(t)$ model (solid curve) in Figure 5 indicates that something changed at $t \approx t_{transition}$. Because the sides of the needle became faceted

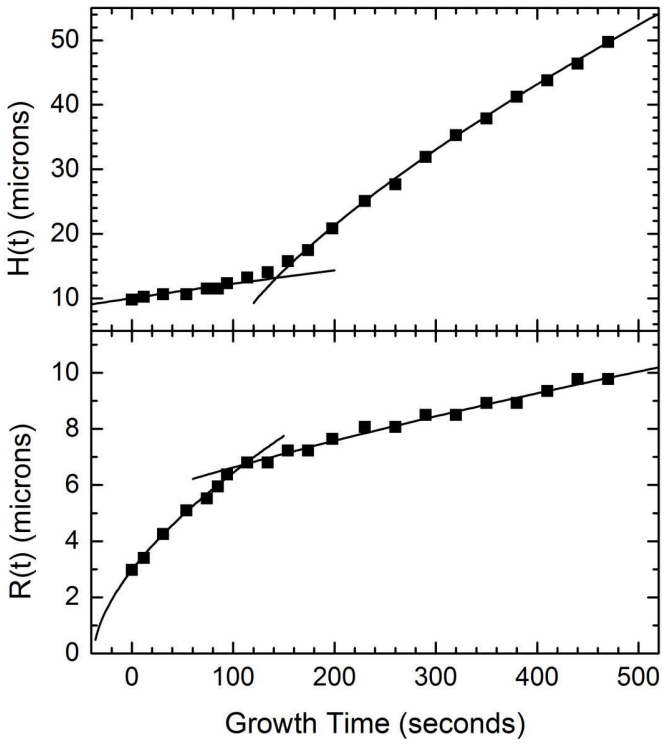

Figure 4: Measurements of the growth of an ice needle at a supersaturation of $\sigma_{center} \approx 1.8$ percent, showing the length of the needle $H(t)$ (top panel) and the needle tip radius $R(t)$ (lower panel) as a function of growth time. A constant length was subtracted from the $H(t)$ measurements to obtain the (arbitrary) starting point $H(t = 0) \approx 10$ μm. Curves were drawn through the data to guide the eye. Note the rather abrupt change in the growth behavior at $t \approx t_{transition} = 130$ seconds.

at about this time, the data indicate that the attachment coefficient on a faceted prism surface does *not* satisfy the inequality $\alpha_{prism} \gg \alpha_{diffcyl}$. Had this inequality been true, the data would have followed the solid curve for $t > t_{transition}$.

When faceted prism surfaces are present for $t > t_{transition}$, we can again make an analytic model of the radial growth rate using Equation 1 with $\alpha_{cyl} = \alpha_{prism}$, giving

$$\frac{dR}{dt} = \frac{\alpha_{diffcyl}\alpha_{prism}}{\alpha_{diffcyl} + \alpha_{prism}} v_{kin}\sigma_{center} \tag{5}$$

Comparing this with Equation 3, we see immediately that the approximate 2x drop in dR/dt at $t \approx t_{transition}$ indicates that $\alpha_{prism} \approx \alpha_{diffcyl}$.

Choosing the slightly model-dependent form $\alpha_{prism}(\sigma_{surface}) = A_{prism} \exp(-\sigma_{0,prism}/\sigma_{surface})$ (for reasons we discuss below), where A_{prism} and $\sigma_{0,prism}$ are constants with $\sigma_{0,prism} = 0.17$ percent

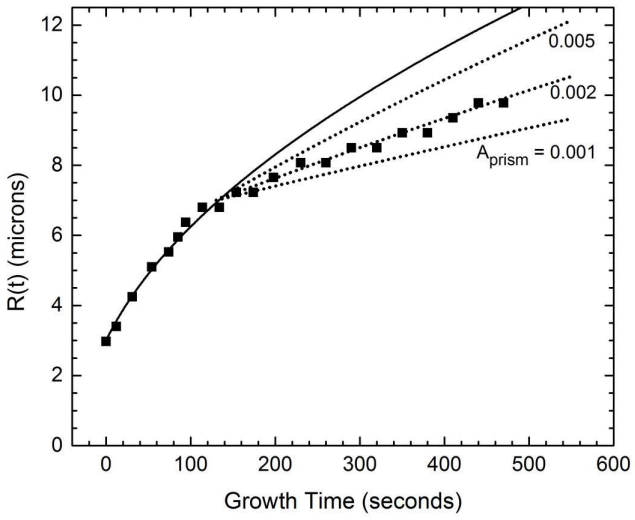

Figure 5: This graph shows the $R(t)$ data in Figure 4 along with several calculated models. The solid curve shows Equation 4 using the measured initial condition $R_0 = R(t_0) = 3$ μm and a small adjustment of σ_{center} to fit the data. This curve describes the data for $t < 130$ seconds, when the prism surfaces are not faceted and therefore $\alpha_{vicinal} \gg \alpha_{diffcyl}$. At later times the prism surfaces are faceted and we cannot assume $\alpha_{prism} \gg \alpha_{diffcyl}$. The dotted curves show three numerical models described in the text, with different A_{prism} values as labeled.

[24], we obtained $\sigma_{surface}$ by solving the equation

$$\sigma_{surface} = \frac{\alpha_{diffcyl}}{\alpha_{diffcyl} + \alpha_{prism}(\sigma_{surface})}\sigma_{center}$$

by iteration, which then allowed us to solve Equation 5 for $R(t)$. Using different assumptions for A_{prism} gave the dotted curves shown in Figure 5, giving a best-fit value of $A_{prism} = 0.002$. Note that using a constant $\alpha_{prism} = 0.002$ gives quite similar results, because the final model yields that $\sigma_{surface}$ is roughly six times larger than $\sigma_{0,prism}$, and therefore $\exp(-\sigma_{0,prism}/\sigma_{surface}) \approx 1$.

It is instructive at this point to examine the supersaturation field $\sigma(r)$ around the growing crystal, again using the infinite-cylinder approximation. The general solution to the diffusion equation around an infinite cylinder is $\sigma(r) = A_1 + A_2 \log(r)$, where A_1 and A_2 are constants determined by the boundary conditions. The two models above for $t < t_{transition}$ and $t > t_{transition}$ give the two $\sigma(r)$ lines shown in Figure 6, where we have indicated the special radii $r = R_{in} = 7$ μm (the crystal surface at $t = t_{transition}$), $r = R_{out} = 75$ μm (the outer boundary used in our numerical models), and $r = R_{far} = 2$ cm (the effective outer boundary in our analytic models, as determined by the supersaturation calibration in [22]).

The supersaturation at R_{far} is given by $\sigma_{far} = \sigma_{center} \approx 1.8$ percent, which is fixed by the temperature profile of the diffusion chamber. Because this temperature profile remained constant as the crystal grew, the value of σ_{far} does not change at $t = t_{transition}$ when the sides of the needle

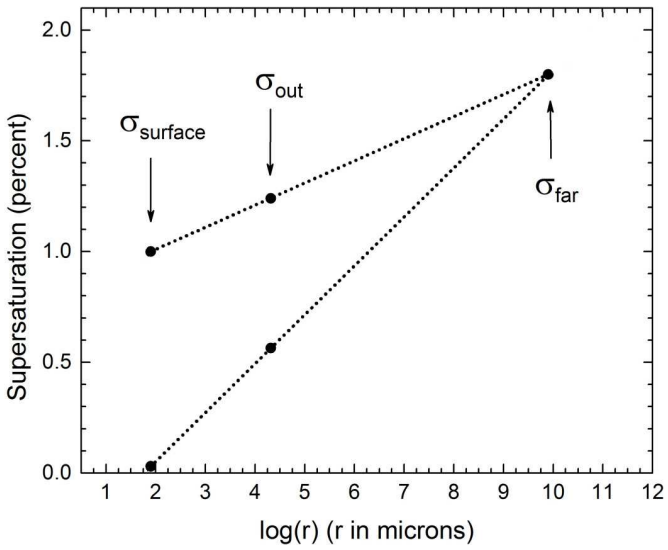

Figure 6: This plot shows the model supersaturation $\sigma(r)$ surrounding the columnar crystal as a function of $\log(r)$, as described in the text. For $t < t_{transition}$, $\alpha_{vicinal} \gg \alpha_{diffcyl}$ and we obtain the lower dotted line, using the known outer boundary condition $\sigma(R_{far}) = \sigma_{far} \approx 1.8$ percent at $R_{far} \approx 2$ cm. For $t > t_{transition}$, the columnar walls are faceted with a much lower $\alpha_{prism} \approx 0.002$, yielding the upper line shown here.

became prism facets.

In contrast, the value of $\sigma_{surface}$ depends on the inner boundary condition at $r = R_{in}$, which does change at $t = t_{transition}$. For times $t < t_{transition}$, we have $\sigma_{surface} \approx (\alpha_{diffcyl}/\alpha_{vicinal})\,\sigma_{center}$, coming from $dR/dt = \alpha_{diffcyl} v_{kin} \sigma_{center} = \alpha_{vicinal} v_{kin} \sigma_{surface}$, which is one form of the inner boundary condition. The fact that $\alpha_{vicinal} \gg \alpha_{diffcyl}$ means that $\sigma(r = R_{in})$ is quite small for $t < t_{transition}$, as shown in Figure 6. Note that the straight lines in the figure connect the known σ values at $r = R_{in}$ and $r = R_{far}$ to give the full solutions $\sigma\,(r) = A_1 + A_2 \log(r)$.

For $t > t_{transition}$, our best fit $A_{prism} = 0.002$ combines with $\alpha_{diffcyl}$ to yield $\sigma_{surface} \approx 1$ percent, yielding the upper dotted line in Figure 6. A key point in Figure 6 is that the drop in α on the sides of the column from $\alpha_{vicinal}$ to α_{prism} at $t \approx t_{transition}$ results in a remarkably large jump in $\sigma_{surface}$, from near zero to about one percent. It is this sudden change in $\sigma_{surface}$ that causes the observed jump in dH/dt.

To model $H(t)$, and to deal with the free end of the column more generally (no longer in the infinite-cylinder approximation) we again use the cylindrically symmetrical cellular automata model described in [18], and the model results are shown with the data in Figure 7. Importantly, these models were not adjusted to fit the data, as all the model inputs were determined by other measurements. For $t < t_{transition}$, we used $\alpha_{vicinal} \approx 0.1$ (the exact value was not important as long as $\alpha_{vicinal} \gg \alpha_{diffcyl}$) and $\alpha_{basal} = \exp(-\sigma_{0,basal}/\sigma_{surf})$ with $\sigma_{0,basal} = 0.8$ percent, as measured in [24]. For $t > t_{transition}$ we used $A_{prism} = 0.002$ from our analytical modeling. The supersaturation

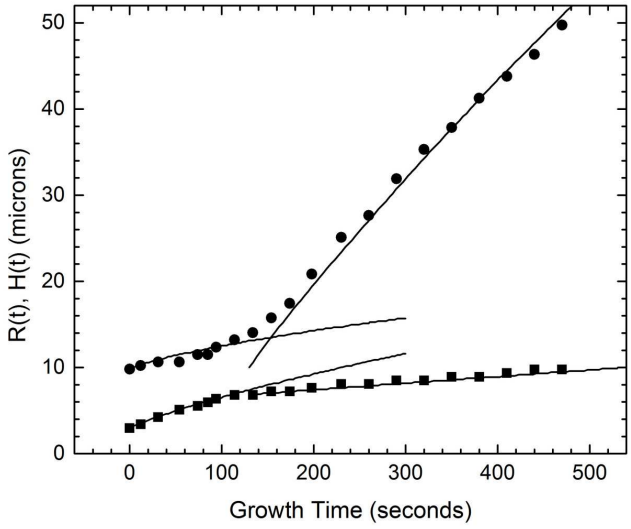

Figure 7: This graph shows the data in Figure 4 along with two numerical models, one for $t < t_{transition} = 130$ seconds (modeling both $R(t)$ and $H(t)$), and a second model for $t > t_{transition}$. Using the basal attachment coefficient measured in [24], together with the parameters determined by our analytic modeling of $R(t)$, yields good agreement with both the $R(t)$ and $H(t)$ data. The change at $t \approx t_{transition}$ arises when the sides of the columnar crystal become faceted, changing the attachment coefficient from $\alpha_{vicinal}$ to $\alpha_{prism} \approx 0.002$. This slows the radial growth rate dR/dt, but also causes a large jump in $\sigma_{surface}$, as shown in Figure 6. This jump then causes the axial growth rate dH/dt to increase by about a factor of four.

at the outer boundary at $r = R_{out} = 75$ μm changed from $\sigma_{out} = 0.6$ percent for $t < t_{transition}$ to $\sigma_{out} = 1.0$ percent for $t > t_{transition}$ seconds, with these values provided by the analytic models shown in Figure 6.

Our essential conclusion from the $H(t)$ modeling shown in Figure 7 is a simple one: the basal attachment coefficient $\alpha_{basal} = \exp(-\sigma_{0,basal}/\sigma_{surf})$ from the low-pressure data in [24] provides good agreement with the needle growth data taken in air. Figure 8 shows that the transitional jump in dH/dt was observed only at intermediate supersaturations.

2.3 Thermal Effects

It is also worth pointing out that thermal effects from latent heating are beginning to become significant at this intermediate supersaturation level. In the infinite-cylinder approximation, latent heating yields a temperature increase of the ice (relative to the far-away air temperature) of [22]

$$\delta T = \frac{B\lambda\rho v R}{\kappa}$$

which gives $\delta T \approx 0.2$ C for $t < t_{transition}$ and $\delta T \approx 0.06$ C for $t > t_{transition}$, not including additional heating from the axial growth. Heating from dH/dt is more difficult to estimate, as it is

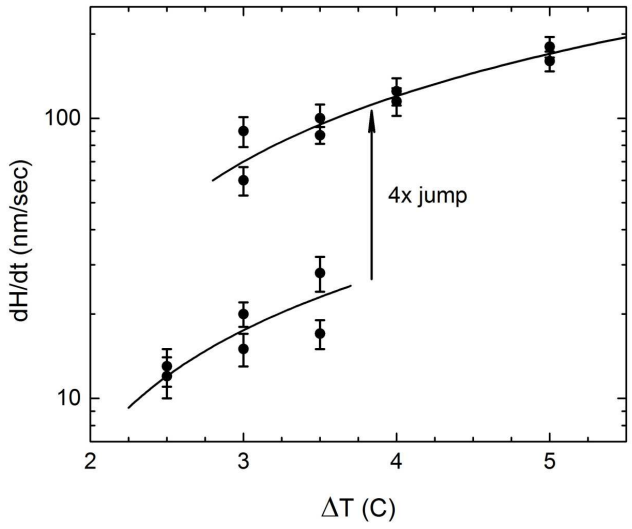

Figure 8: This graph shows the axial growth rate dH/dt for several needle crystals covering a range of ΔT. For $\Delta T = 3$ and 3.5 C, dH/dt was measured both before and after the transition caused by faceting of the prism surfaces. At higher and lower ΔT, no jump in dH/dt was observed.

concentrated at the needle tip, so heat is conducted down the needle and then into the surrounding air. Nevertheless, we estimate that heating effects in this crystal are dominated by heating from radial growth, as the tip area is quite small. While we did not solve the full particle+heat diffusion problem, our approximate analysis suggests that heating created a relatively small correction to the above analysis, and does not alter our conclusions.

2.4 Growth at High Supersaturation

Raising σ_{center} still higher, Figure 1 shows an additional test crystal grown at $\Delta T = 5$ C, for which $\sigma_{center} \approx 3.7$ percent. At this higher supersaturation, the faceted columnar morphology includes a conical hollowed structure at the tip, which developed as the needle grew longer. Moreover, the initial positive taper of the column almost immediately reversed to an overall negative taper, with R largest at the tip, as is seen in Figure 1. Measurements of $R(t)$ show a simple $R \sim t^{1/2}$ behavior, with no obvious transitions. The observations thus indicate that $\alpha_{prism} > \alpha_{diffcyl} \approx 0.002$ because the top prism terrace at the end of the needle is growing at essentially the same velocity as the vicinal surfaces making up the negative taper. Beyond this inequality, however, we cannot determine α_{prism} from the columnar growth.

At still higher σ_{center}, the prism facets disappear entirely, and the morphology transitions into "fishbone" dendrites [23, 21] for $\sigma_{center} > 15$ percent. The disappearance of prism facets indicates $\alpha_{prism} \approx 1$ at these high supersaturations. However, heating plays a larger role at higher supersaturations as well, making it necessary to better incorporate heating effects into our growth models before we can draw reliable conclusions.

3 Discussion

Our principal conclusion from this work is that $\alpha_{prism} \approx 0.002$ at temperatures near -5 C in air at $p_{air} = 1$ bar. This statement strictly applies for a surface supersaturation near $\sigma_{surface} \approx 1$ percent, with an overall uncertainty in α_{prism} of roughly a factor of two. Similar values of α_{prism} were obtained over a larger range of $\sigma_{surface}$ in [25], in general agreement with the current work. We believe these data provide the most accurate quantitative determinations of α_{prism} to date, supporting many decades of morphological observations of the growth of slender columnar ice crystals in air near -5 C.

This exceptionally low value of α_{prism} is strongly inconsistent with our previous measurment of $\alpha_{prism} \approx 0.15 \exp(-\sigma_{0,prism}/\sigma_{surface})$ with $\sigma_{0,prism} \approx 0.17$ percent, which we obtained at $p_{air} \approx 0.01$ bar. We believe that both these measurements are accurate, as both were done in well controlled conditions, giving considerable attention to diffusion modeling and eliminating systematic errors. The clear descrepancy in the measurements thus forces us to the conclusion that α_{prism} depends on p_{air}, dropping by nearly two orders of magnitude as p_{air} is increased from 0.01 to 1 bar.

There have been other indications that α_{prism} is quite small near -5C, and others have speculated that the ice attachment coefficients might depend on p_{air}. Howver, interpreting many of the older ice-growth observations into a quantitative measure of α_{prism} has been problematic. Systematic errors, especially relating to precise modeling of particle diffusion, have made it difficult to accurately relate growth rates to attachment coefficients [26, 27]. In contrast, the growth transition of the intermediate-σ_{center} crystal presented above makes an especially strong case for $\alpha_{prism} \approx 0.002$.

In a previous report we incorrectly assumed that α_{prism} was not affected by p_{air}, which then led us to the conclusion that changes in α_{basal} were necessary to explain the growth of columnar crystals at -5 C [28]. As we stated in [28], this assumption was consistent with the data available at that time, but we also wrote that we could not "positively exclude that there may be some pressure dependence in α_{prism}." The new results presented here negate this important assumption made in [28], and thus negate our conclusion that changes in α_{basal} with terrace thickness are required to explain the growth of columnar crystals near -5 C. The data now suggest that no changes in α_{basal} with terrace thickness are necessary, and further suggest that α_{basal} does not change with p_{air}. However, the data still support our hypothesis that α_{prism} does change with terrace thickness near -15 C [29, 30].

We can offer no microscopic physical model to explain the measured $\alpha_{prism}(\sigma_{surface}, p_{air})$, especially the dependence on p_{air}. We considered the possibility that $\sigma_{0,prism}$ increased with p_{air}, as this could yield the small α_{prism} values measured. Such a model would yield strong changes in α_{prism} as a function of $\sigma_{surface}$, however, and this behavior seems to be excluded by other measurements [25]. Moreover, we are inclined to think, on physical grounds, that the presence of air at the crystal surface should not change the step energy of a prism terrace, and thus should not change $\sigma_{0,prism}$ from the value $\sigma_{0,prism} \approx 0.17$ percent measured at $p_{air} \approx 0.01$ bar.

Given these considerations, we suggested the separated functional form

$$\alpha_{prism} = A_{prism}(\sigma_{surface}, p_{air}) \exp(-\sigma_{0,prism}/\sigma_{surface})$$

described above, keeping $\sigma_{0,prism} \approx 0.17$ percent. The data then suggest $A_{prism} \approx 0.002$ for $\sigma_{surface} \approx 1$ percent, and that A_{prism} increases with higher $\sigma_{surface}$, eventually becoming $A_{prism} \approx 1$ when $\sigma_{surface} \gg 1$ percent. This low-$\sigma_{0,prism}$ model makes a prediction that, for very low $\sigma_{surface}$, we should find $\alpha_{prism} \approx 0.002 \exp(-\sigma_{0,prism}/\sigma_{surface})$, and this could be tested with additional

measurements. Without a better understanding of the molecular processes underlying α_{prism}, or more definative measurements, we cannot carry the discussion much further.

These new revelations change our overall picture of ice growth dynamics. The data now suggest that α_{basal} is described simply by the measurements in [24], with no depedence on p_{air}, and no dependence on terrace width. All of the peculiar behavior is now placed on the prism facet, with α_{prism} depending strongly on p_{air} at $T = -5$ C, with a complex dependence on $\sigma_{surface}$ as well. Moreover, we have found in other measurments that α_{prism} depends strongly on terrace width near $T = -15$ C. All this peculiar behavior may be related to the onset of surface roughening on the prism facet, which appears to happen gradually over the temperature range $-1 > T > -10$ C [24].

Although we are making progress toward a comprehensive model of ice growth, our picture remains phenomenologically complex. We still possess little real understanding of the fundamental molecular processes responsible for the observed behavior of the attachment coefficients with temperature, supersaturaion, and background air pressure.

References

[1] U. Nakaya. *Snow Crystals*. Harvard University Press: Cambridge, 1954.

[2] B. J. Mason, G. W. Bryant, and A. P. Van den Heuvel. The growth habits and surface structure of ice crystals. *Phil. Mag.*, 8:505–526, 1972.

[3] D. Lamb and W. D. Scott. Linear growth rates of ice crystals grown from the vapor phase. *J. Cryst. Growth*, 12:21–31, 1972.

[4] T. Kuroda and R. Lacmann. Growth kinetics of ice from the vapour phase and its growth forms. *J. Cryst. Growth*, 56:189–205, 1982.

[5] W. Beckmann, R. Lacmann, and A. Blerfreund. Growth rates and habits of ice crystals grown from the vapor phase. *J. Phys. Chem.*, 87:4142–4146, 1983.

[6] Jon Nelson and Charles Knight. Snow crystal habit changes explained by layer nucleation. *J. Atmos. Sci.*, 55:1452–1465, 1998.

[7] K. G. Libbrecht. The physics of snow crystals. *Rep. Prog. Phys.*, 68:855–895, 2005.

[8] M. Bailey and J. Hallett. Growth rates and habits of ice crystals between -20c and -70c. *J. Atmos. Sci.*, 61:514–544, 2004.

[9] Matthew Bailey and John Hallett. A comprehensive habit diagram for atmospheric ice crystals: confirmation from the laboratory, airs ii, and other field studies. *J. Atmos. Sci.*, 66:2888–2899, 2009.

[10] Charles A. Knight. Ice growth from the vapor at -5 c. *J. Atmos. Sci.*, 69:2031–2040, 2012.

[11] Matthew Bailey and John Hallett. Ice crystal linear growth rates from -20 to -70c: Confirmation from wave cloud studies. *J. Atmos. Sci.*, (69):390–402, 2012.

[12] Minoru Maruyama. Roughening transition of prism faces of ice crystals grown from melt under pressure. *J. Cryst. Growth*, 275:598–605, 2005.

[13] J. Nelson. Growth mechanisms to explain the primary and secondary habits of snow crystals. *Phil. Mag.*, 81:2337–2373, 2001.

[14] Toshio Kuroda and Takehiko Gonda. Rate determining processes of growth of ice crystals from the vapour phase - part ii: Investigation of surface kinetic processes. *J. Meteor. Soc. Jap.*, 62:563–572, 1984.

[15] C. A. Reiter. A local cellular model for snow crystal growth. *Chaos, Solitons, and Fractals*, 23:1111–1119, 2005.

[16] Janko Gravner and David Griffeath. Modeling snow crystal growth ii: A mesoscopic lattice map with plausible dynamics. *Physica D*, 237:385–404, 2008.

[17] Janko Gravner and David Griffeath. Modeling snow-crystal growth: A three-dimensional mesoscopic approach. *Phys. Rev. E*, 79:011601, Jan 2009.

[18] Kenneth G. Libbrecht. Quantitative modeling of faceted ice crystal growth from water vapor using cellular automata. *J. Computational Methods in Phys.*, (ID-174806), 2013.

[19] Kenneth G. Libbrecht. Incorporating surface diffusion into a cellular automata model of ice growth from water vapor. *arXiv:*, (1509.08543), 2015.

[20] James G. Kelly and Everett C. Boyer. Physical improvements to a mesoscopic cellular automaton model for three-dimensional snow crystal growth. *arXiv:*, (1308.4910), 2013.

[21] Kenneth G. Libbrecht. A dual diffusion chamber for observing ice crystal growth on c-axis ice needles. *arXiv:*, (1405.1053), 2014.

[22] Kenneth G. Libbrecht. Measurements of cylindrical ice crystal growth limited by combined particle and heat diffusion. *arXiv:*, (1602.02683), 2016.

[23] Kenneth G. Libbrecht. Identification of a novel 'fishbone' structure in the dendritic growth of columnar ice crystals. *arXiv:*, (0912.2522), 2009.

[24] Kenneth G. Libbrecht and Mark E. Rickerby. Measurements of surface attachment kinetics for faceted ice crystal growth. *J. Crystal Growth*, (377):1–8, 2013.

[25] K. G. Libbrecht and H. M. Arnold. Measurements of ice crystal growth rates in air at -5 c and -10 c. *arXiv:*, (0912.2518), 2009.

[26] K. G. Libbrecht. A critical look at ice crystal growth data. *arXiv:*, (cond-mat/0411662), 2004.

[27] Kenneth G. Libbrecht. Managing systematic errors in ice crystal growth experiments. *arXiv:*, (1208.5064), 2012.

[28] Kenneth G. Libbrecht. Toward a comprehensive model of snow crystal growth dynamics: 2. structure dependent attachment kinetics near -5 c. *arXiv:*, (1302.1231), 2013.

[29] K. G. Libbrecht. An edge-enhancing crystal growth instability caused by structure-dependent attachment kinetics. *arXiv:*, (1209.4932), 2012.

[30] Kenneth G. Libbrecht. Toward a comprehensive model of snow crystal growth dynamics: 4. measurements of diffusion-limited growth at -15 c. *arXiv:*, (1302.1231), 2013.